Composition and Dimension Dependent Static and Dynamic Stabilities of Inorganic Mixed Halide Antimony Perovskites

Jack Yang[*]

Materials and Manufacturing Futures Institute, School of Material Science and Engineering,

University of New South Wales, Sydney, New South Wales 2052, Australia

E-mail: jianliang.yang1@unsw.edu.au

Abstract

Halide intermixing is an important approach to stabilise halide perovskite in the phase that gives the best optoelectronic properties, whereas replacing Pb is critical for eliminating the material toxicity to meet the requirements for domestic applications. Recently, all–inorganic lead–free $Cs_3Sb_2I_9$ emerges as a promising lead–free absorber, with its optoelectronic properties being further controllable by manipulating its structural dimensionality (0D or 2D) via composition engineering. In particular, superior photoconversion efficiency (up to 5 %) under indoor illumination with high photostabilities have been demonstrated experimentally in 2D $Cs_3Sb_2Cl_yI_{9-y}$. To gain a more thorough understanding on how the properties of this family of materials are controlled by their chemistry and dimensionality, here, we employ density functional theory calculations to explore the phase stability, structural and electronic dynamics of $Cs_3Sb_2X_yI_{9-y}$ (X=Br and Cl) across 74 different combinations of composition/dimensionality. The results show that $Cs_3Sb_2X_yI_{9-y}$ solid solutions are predominantly stabilised by configurational entropy rather than enthalpy. In stark contrast to cubic inorganic lead/tin halides perovskites, $Cs_3Sb_2X_yI_{9-y}$ are dynamically more stable at 300 K, as reflected by their low vibrational anharmonicities, the values of which also exhibit weak compositional dependency. This consequentially reduces the strength of electron–phonon couplings, thus enhancing the photoexcited carrier lifetime in these materials, which further demonstrates their promising potential to be integrated into indoor photovoltaic devices.

Introduction

Developing efficient new photovoltaic materials is an important pathway to solve the global problems of energy shortage and environmental pollution, in order to achieve a sustainable development of human society. During the past decade, lead halide perovskites[1–3] emerge as a new group of materials for solar photovoltaics due to their high photoconversion efficiency of ~ 25 % and solution processibility, but their domestic applications are severely impeded by the lead toxicity.[4,5] As such, there is a large driving force to develop lead–free perovskites photoabsorbers with comparable chemical/physical properties and device performance.[6–8] Fortunately, the versatility in perovskite chemistry means a wide chemical space can be explored to discover materials that can fulfil such a requirement,[9–11] among which, antimony–based perovskite has been identified as a promising choice for the low–toxicity and high earth–abundance of Sb.

However, due to the trivalency of Sb, antimony halides typically do not form ABX_3–type perovskites but are confined to the stoichiometry of $A_3B_6X_9$ (X=Cl, Br or I). As a result, inorganic $Cs_3Sb_6X_9$ occurs as 'low–dimensional' perovskites with either 0D (face–sharing) or 2D (corner–sharing) connectivities of SbX_6 octahedra (Fig. 1). Whilst it provides us an interesting system to examine the dimensional dependent photophysics of halide perovskites, the more commonly occurring 0D polymorph (for iodide) is a large indirect band gap (2.2–2.5 eV) semiconductor with poor electrical conductivities that are not suitable for solar photovoltaics. Hence stabilising the 2D polymorph has been a key driving forces for the efforts in developing antimony halide perovskites as the workable lead–free alternative.
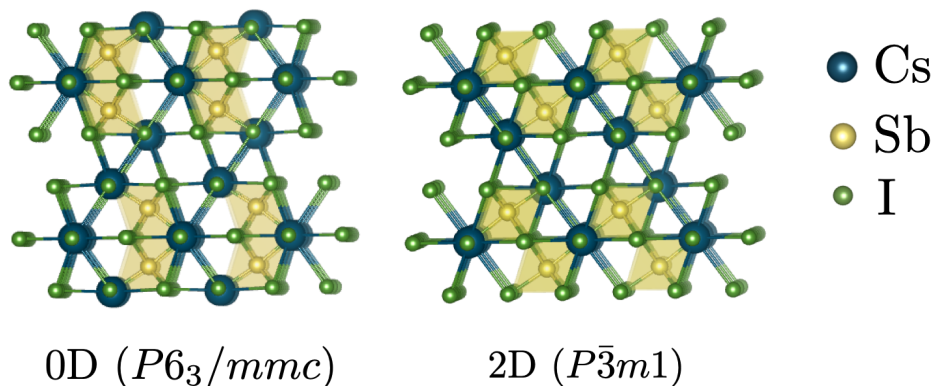

0D ($P6_3/mmc$)   2D ($P\bar{3}m1$)

Figure 1: Crystal structures of 0D and 2D lead–free halide perovskite $Cs_3Sb_2I_9$.

Temperature–controlled selective synthesis of 0D and 2D $Cs_3Sb_6I_9$ at 150 °C and 250 °C, respectively, was first reported in 1997 by Yamada *et al*.[12] With a surge of interests in perovskite photovoltaics, similar approach has been adopted more recently to synthesise 2D $Cs_3Sb_6I_9$ and demonstrated its superior photovoltaic performance compared with its 0D polymorph.[13,14] Chemically, halide intermixing is another effective strategy to stabilise a particular perovskite phase with suitable band gap for solar

photoabsorption at the operating temperature. For example, cubic perovskite $CsPbI_3$ with a suitable band gap of 1.73 eV as solar absorber is prone to phase transform into its tetragonal phase of larger band gap at room temperature, such problem can be mitigated by mixing I with a small amount of Br/Cl. [15–19] Similar strategy has also been explored recently to stabilise the 2D phase of antimony perovskites, mostly focusing on Cl/I intermixing. In the earliest attempt by Jiang *et al.*, [20] hybrid perovskite $MA_3Sb_2Cl_xI_{9-x}$ (MA=methylammonium) in its 2D phase was synthesised via solution processing. With higher structural stabilities in fully inorganic perovskites, more recently, 2D mixed halide $Cs_3Sb_2Cl_xI_{9-x}$ thin films were fabricated. [21,22] Even though the as–synthesised materials were still of a band–gap value between 1.9 to 2.0 eV, it is demonstrated [23] to possess one of the highest ($\sim 62\%$) spectroscopy limited maximum efficiency under fluorescence/white–light irradiation, as well as high resistance against light–induced halide segregation. The latter is caused by the presence of soft phonon vibrations in perovskites that couple strongly to their electronic subsystems. [24–27] It is a critical problem to be overcome in perovskite photovoltaics for enhancing their long–term stability. Combining with the low toxicity of antimony, the above findings further demonstrate this material is indeed suitable to be applied as indoor photovoltaic power generator for wearable electronics.

With these in mind, there is a fundamental interest for us to thoroughly understand how halide intermixing affects the physical properties of low–dimensional inorganic antimony halide perovskites, in order to guide future works on optimising their device performances. As such, hereby, we employ density functional theory (DFT) simulations to systematically examine the composition and dimension dependent thermodynamic stabilities, as well as the ionic and electronic dynamics of mixed halide $Cs_3Sb_2X_yI_{9-y}$ (X=Br, Cl) solid solution. It is found that Cl intermixing provides significantly larger driving forces to stabilise the 2D structures of $Cs_3Sb_2X_yI_{9-y}$ compared to Br, and configurational entropy plays the dominating contributions in stabilising these solid solutions at low Br/Cl concentrations. Both 0 K lattice dynamic and room–temperature *ab initio* molecular dynamic simulations reveal significantly lower degree of 'vibrational anharmonicity' [28] in $Cs_3Sb_2X_yI_{9-y}$, with dependence on both the chemical composition and structural dimensionality, compared with cubic lead or tin halide perovskites. [29] Consequentially, this weakens the electron–phonon coupling strengths in the material, which can be one of the main reasons behind the experimentally observed high photostability of $Cs_3Sb_2X_yI_{9-y}$ thin films.

Methodologies

Configuration samplings for solid solutions

An $(1 \times 1 \times 1)$ and $(2 \times 1 \times 1)$ supercell model is first built for 0D and 2D $Cs_3Sb_2I_9$, respectively. This gives 18 iodine atoms in the supercell, which are to be randomly replaced by y ($1 \leq y \leq 18$) bromine or chlorine atoms for constructing the atomistic models of solid solutions. The latter is achieved using the

3

⁷⁷ functionality of creating substituted structures as implemented in Pymatgen[30] package. After filtering
⁷⁸ out the duplicated structures, we retain 522 (628) and 499 (623) configurations of solid solutions for 0D
⁷⁹ (2D) $Cs_3Sb_2Cl_yI_{9-y}$ and $Cs_3Sb_2Br_yI_{9-y}$ in total.

DFT calculations at 0 K

⁸¹ For every configuration generated, its atomic positions and lattice constants are fully optimised using
⁸² DFT as implemented in the VASP[31] code. The exchange–correlation interaction energies are ap-
⁸³ proximated with the Perdew–Burke–Ernzerhof (PBE)[32] functional, whereas the atom–centred electron
⁸⁴ densities are expanded with the standard projector–augmented–wave (PAW)[33] method at 350 eV pseu-
⁸⁵ dopotential cut–off. Geometry optimisations are performed with a uniform grid spacing of 0.04 Å^{-1} for
⁸⁶ the Monkhorst–Pack k–point grid, and are terminated when the total energy change is less than 10^{-4}
⁸⁷ eV. The energetically most stable configuration for each composition is then extracted, the dynamics
⁸⁸ and electronic properties of which are further examined, as detailed in the following.

Harmonic phonon calculations

⁹⁰ 0 K harmonic phononic properties are calculated using the finite–displacement approach as implemented
⁹¹ in the PHONOPY[34] code. A $(2 \times 2 \times 1)$ supercell of an optimised $Cs_3Sb_2X_yI_{9-y}$ structure is used for
⁹² generating the atom–displaced structures. The electronic self–consistent fields are converged at Γ–point
⁹³ only with `ACCURATE` being set for the precision tag. The GW version of the pseudopotential is used,
⁹⁴ which improves the convergence of the electronic self–consistent cycles. All other options remain un-
⁹⁵ changed as detailed in the previous section. This enables us to extract the second–order force–constants
⁹⁶ $\Phi_{ij}^{\alpha\beta}$, which is critical for the subsequent quantification of materials' vibrational anharmonicities.

Ab initio molecular dynamics (MD)

⁹⁸ Room–temperature (300 K) structural dynamics of $Cs_3Sb_2X_yI_{9-y}$ are investigated with *ab initio* MD
⁹⁹ using VASP. The simulation supercells and DFT parameters employed are the same as those for the
¹⁰⁰ phonon calculations. Each configuration is first equilibrated for 100 fs to the target temperature using
¹⁰¹ the velocity scaling algorithm. Subsequent production run is performed to generate a 1.6 ps trajectory
¹⁰² with 1 fs step size under the NVT ensemble using an Andersen thermostat with a collision rate of
¹⁰³ 0.5. Structural analysis are performed on MD snapshots collected every 1 fs. To extract the electronic
¹⁰⁴ dynamics of selected compositions, the electronic band gap energies are determined from calculated
¹⁰⁵ band structure for each one of the 1600 MD frames. To reduce the overall computational costs, based
¹⁰⁶ on the band structures for $Cs_3Sb_2I_9$ at 0 K, we calculated the band dispersion along the $\Gamma - K$ direction
¹⁰⁷ only, from a pre–converged charge density at Γ–point.

Quantifying vibrational anharmonicity

Ab initio MD simulations are capable of capturing the full vibrational anharmonicity in materials. Fundamentally, the vibrational behaviour is determined by the crystal potential $\mathcal{V}(\mathbf{R})$ as a function of atomic position $\mathbf{R}$. In order to quantify the degree of vibrational anharmonicity in $Cs_3Sb_2X_yI_{9-y}$ at 300 K, we employ the 'anharmonicity score' (σ) as recently proposed by Knoop *et al.*[28] Mathematically, σ is defined as:

$$\sigma = \sqrt{\frac{\sum_{j,\alpha} \left\langle \left(F_{j,\alpha}^A \right)^2 \right\rangle_T}{\sum_{j,\alpha} \left\langle \left(F_{j,\alpha} \right)^2 \right\rangle_T}}. \tag{1}$$

Here, $F_{j,\alpha}$ is the force from *ab initio* MD on atom j along α Cartesian direction. $\langle \cdot \rangle_T$ represents thermodynamic averaging over all atoms across the entire MD trajectory. $F_{j,\alpha}^A$ is the corresponding anhmarmonic component of the atomic force, which is given by the difference between $F_{j,\alpha}$ and its harmonic component $F_{j,\alpha}^{(2)}$ at displacement $\Delta\mathbf{R}_{j,\alpha}$ as sampled from MD, and can be calculated via $F_{j,\alpha}^{(2)} = -\sum_{k,\beta} \Phi_{\alpha\beta}^{jk} \Delta\mathbf{R}_{j,\alpha}$, in which the harmonic force–constant $\Phi_{\alpha\beta}^{jk}$ is obtained from the result of harmonic phonon calculation at 0 K. As such, $\sigma = 0$ can only be observed in strictly harmonic systems where $\mathcal{V}(\mathbf{R})$ is a parabolic function.

Results and discussions

Thermodynamic stabilities of $Cs_3Sb_2X_yI_{9-y}$ solid solutions

As a pure compound, $Cs_3Sb_2I_9$ prefers the 0D polymorph over the 2D one. The relative stability between these two polymorphs are affirmed by our DFT results, which show the 0D polymorph is more stable by 4 meV/atom in ΔH_f (the formation enthalpy of the compound, measured with respect to the energies of its constituent atoms). Mixing iodide with chloride forming $Cs_3Sb_2Cl_yI_{9-y}$ solid solution has been demonstrated to be a viable approach to stabilise the 2D structure,[21,35] but less focus is on $Cs_3Sb_2Br_yI_{9-y}$. This can be explained by the fact that (a) ΔH_f for $Cs_3Sb_2X_9$ in either 0D or 2D structure decrease in the order of I>Br>Cl, and (b) ΔH_f for 2D $Cs_3Sb_2Cl_9$ is 10 meV/atom lower than its 0D structure, compared to just 3 meV/atom difference between the 2D and 0D structures for $Cs_3Sb_2Br_9$. This means that the thermodynamic driving force to stabilise 2D perovskites is much higher provided by I/Cl intermixing, rather than the I/Br one. Nevertheless, all these energy differences are found to be smaller than the thermal energy (26 meV) at 300 K.

The above findings suggest that chemical pressure is a critical driving force for phase transformation in $Cs_3Sb_2X_yI_{9-y}$ solid solutions. To further examine this effect in details, Fig. 2 plots the composition
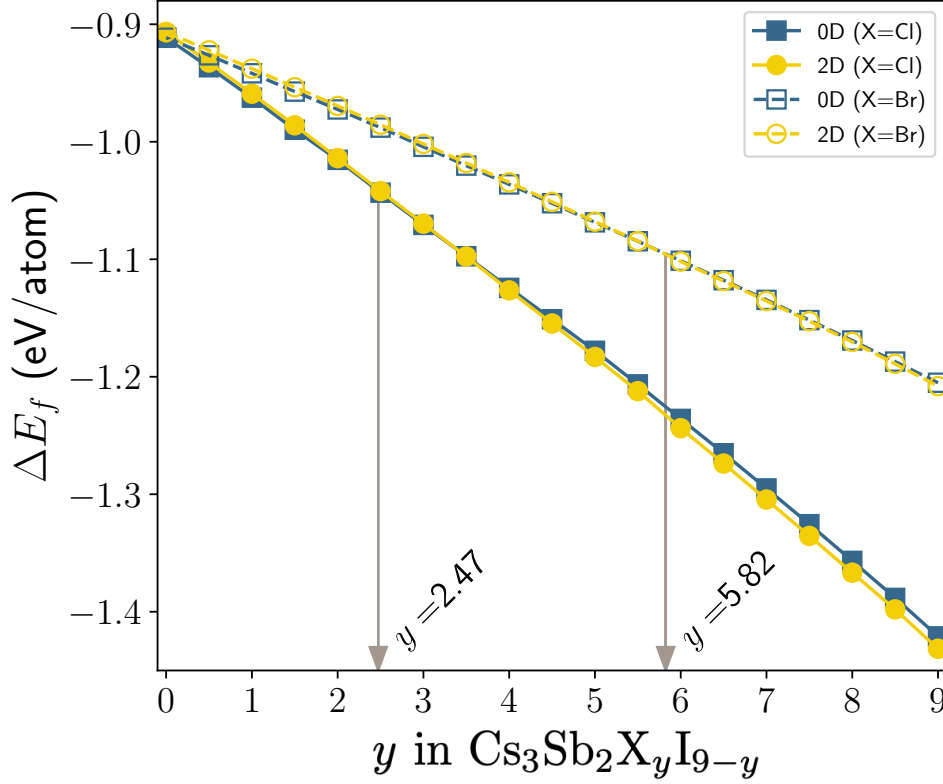
Figure 2: Composition–dependent formation enthaplies (ΔH_f) for 0D and 2D $Cs_3Sb_2X_yI_{9-y}$ (X=Cl and Br). At each composition, ΔH_f is averaged over ΔH_f's for all solid solution structures calculated with that composition. The vertical arrows mark the critical compositions at which both 0D and 2D $Cs_3Sb_2X_yI_{9-y}$ solid solutions have identical ΔH_f for a given X, beyond which the 2D perovskites become more stable than the 0D ones. The critical points are found by first fitting $\Delta H_f(y)$ to Eq. (2), and then solving the equation $\Delta H_f^{0D}(y) = \Delta H_f^{2D}(y)$.

dependency of formation enthalpies $\Delta H_f(y)$ for $Cs_3Sb_2X_yI_{9-y}$ in both 0D and 2D phases. The significantly lower ΔH_f for $Cs_3Sb_2Cl_9$ translates into a much steeper change in ΔH_f with respect to the Cl content in $Cs_3Sb_2Cl_yI_{9-y}$ solid solutions. Since the function relating the physical properties of (halide perovskite) alloy to its composition could exhibit 'bowing effect' originated from subtle structural relaxations, and charge transfers between ions occupying the same type of lattice sites,[36,37] we fit $\Delta H_f(y)$ to the following quadratic relationship:

$$\Delta H_f(y') = by'(1 - y') -$$
$$y'\Delta H_f[Cs_3Sb_2X_9] - (1 - y')\Delta H_f[Cs_3Sb_2I_9], \quad (2)$$

in which b is the so–called 'bowing parameter', and $y' = y/9$. This gives the b values of 0.0608 (0.0577) and 0.0253 (0.0259) for 0D (2D) $Cs_3Sb_2Cl_yI_{9-y}$ and $Cs_3Sb_2Br_yI_{9-y}$, respectively, indicating that the bowing effect in the formation energy is very weak but nonetheless exists. The larger b values obtained

6

for chloride compared to bromide are in agreement with larger mismatch in electronegativities between Cl/I pair, as compared to the Br/I pair, further indicating that the thermodynamic stabilities are strongly affected by the electronic characters of the $Cs_3Sb_2X_yI_{9-y}$ solid solutions. High stabilities of chloride–containing pervoskites could be attributed to the large electronegativity of chloride in enhancing the charge transfer to Cl^- from other ions.

The critical halide composition y_c, at which the 0D→2D phase transformation occurs, can be obtained by solving for y_c after equating the fitted equations of $\Delta H_f(y')$ [Eq. (2)] for the 0D and 2D structures with the same halide X. These phase transition points are annotated in Fig. 2. It further leads us to discover that the critical point for chlorides is at $y_c = 2.47$, which is less than half of the value for bromides ($y_c = 5.82$). Since the bowing parameters b for $\Delta H(y)$ are very similar between 0D and 2D structures of $Cs_3Sb_2Cl_yI_{9-y}$ and $Cs_3Sb_2Br_yI_{9-y}$, the larger difference in ΔH_f between 0D and 2D $Cs_3Sb_2Cl_9$ should be the predominant driving force for $Cs_3Sb_2Cl_yI_{9-y}$ to transform from 0D into 2D structures at a smaller y_c.

We note that experimentally, $Cs_3Sb_2Cl_yI_{9-y}$ was found to adopt 2D structures when y is between 3.8–4,[21,35] which is in the regime where 2D structures are found to be more stable according to our theoretical results. However, Peng *et al.*[35] also found that for $y > 4$, the mixed halide sample no longer existed as solid solution. This requires us to further examine the thermodynamics of halide intermixing in $Cs_3Sb_2X_yI_{9-y}$ solid solutions, which are detailed as following.

We calculate the composition–dependent mixing enthalpy $\Delta H_{mix}(y)$ for the reaction

$$y'Cs_3Sb_2X_9 + (1 - y')\,Cs_3Sb_2I_9 \rightarrow Cs_3Sb_2X_yI_{9-y}$$

as

$$\Delta H_{mix}(y) = E[Cs_3Sb_2X_yI_{9-y}] - y'E[Cs_3Sb_2X_9] - (1 - y')\,E[Cs_3Sb_2I_9], \tag{3}$$

in which $E[\cdot]$ represents the total energy of a given structure obtained from DFT. Similarly, the temperature–dependent mixing free energies $\Delta G_{mix}(y, T)$ are calculated as[38]

$$\Delta G_{mix}(y) = G[Cs_3Sb_2X_yI_{9-y}] - y'G[Cs_3Sb_2X_9] - (1 - y')\,G[Cs_3Sb_2I_9], \tag{4}$$

where $G[\cdot]$ is the configurational free energy for a solid with halide composition of y, and can be obtained via the bridging relationship

$$G_{conf}(y, T) = -k_B \ln Z(y, T), \tag{5}$$

7

where k_B is the Boltzmann constant, and $Z(y, T)$ is the partition function[39]

$$Z(y, T) = \sum_{n=1}^{N} g_n \exp\left(-\frac{E_n}{k_B T}\right). \tag{6}$$

Here, g_n is the degeneracy factor for the n–th configuration and E_n is the 0 K DFT total energy. While it is possible to further include the vibrational entropic contributions to the total free energies,[40] our previous work[29] demonstrated that it did not lead to a fundamental change in the trend of composition–dependent ΔG_{mix} for $Cs(Pb_x Sn_{1-x})X_3$ solid solutions, hence its contributions are excluded in the present investigation. Finally, in Eqs. (3) and (4), the polymorphous end–points are used,[41,42] meaning that the total energies of the pure compounds are calculated with fully relaxed supercells of the same size as for the solid solutions.

Composition dependent ΔH_{mix} for 0D and 2D $Cs_3Sb_2X_yI_{9-y}$ are presented in the top two rows of Fig. 3. Unlike solid solutions of $CsPbI_yBr_{3-y}$, which was found to be enthalpically stable,[43] this is not the case for low–dimensional antimony perovskites with mixed halide compositions. Between the 0D and 2D structures of a given halide X, there is no large difference in either the shape of the distribution for ΔH_{mix}, nor the maximum ΔH_{mix} values attainable at each halide concentration. This is because, rather than the structural dimensionality, it is the 'short–ranged' bonding environments and strengths are similar in both 0D and 2D polymorphs, which determine the formation thermodynamics in these materials. Chemically, Fig. 3 shows that ΔH_{mix} for $Cs_3Sb_2Cl_yI_{9-y}$ are systematically ~ 3 times larger than ΔH_{mix} for $Cs_3Sb_2Br_yI_{9-y}$. The above observations better reflect the larger up–bowing effect (reflected by positive b's in Eq. 2) observed in $\Delta H_f(y')$ for $Cs_3Sb_2Cl_yI_{9-y}$, because $\Delta H_{mix}(y')$ can be obtained from $\Delta H_f(y')$ [Eq. 2] by subtracting every point with $y' E[Cs_3Sb_2X_9] + (1 - y') E[Cs_3Sb_2I_9]$, meaning the bowing behaviour of ΔH_f is fundamentally governed by the compositional dependency of ΔH_{mix}.

Nevertheless, it should be noticed that all ΔH_{mix} are smaller than the thermal energy at 300 K, suggesting that under normal operating conditions, thermal fluctuations may drive the $Cs_3Sb_2X_yI_{9-y}$ solid solutions to quickly interconvert between different dopant configurations, hence they may be stabilised entropically. This is indeed reflected in Fig. 3(e–f) which show that the mixing free energies $\Delta G_{mix}(y)$ are negative across all halide compositions as temperature increases. The differences in $\Delta G_{mix}(y)$ between 2D and 0D perovskites are generally small except for a few compositions, where the 0D structures are less stable. For both cases of X=Cl and Br, pronounced minima in $\Delta G_{mix}(y)$ occur at y between 2 to 3. This may explain why $Cs_3Sb_2Cl_yI_{9-y}$ was difficult to form solid solution with $y > 4$ as observed in experiments:[35] Solid solutions with higher halide mixing ratios prefer to phase segregate driven by enthapies. During this process, localized regions of low mixing concentrations may form, which are then trapped in the free–energy minimum by configurational entropy.
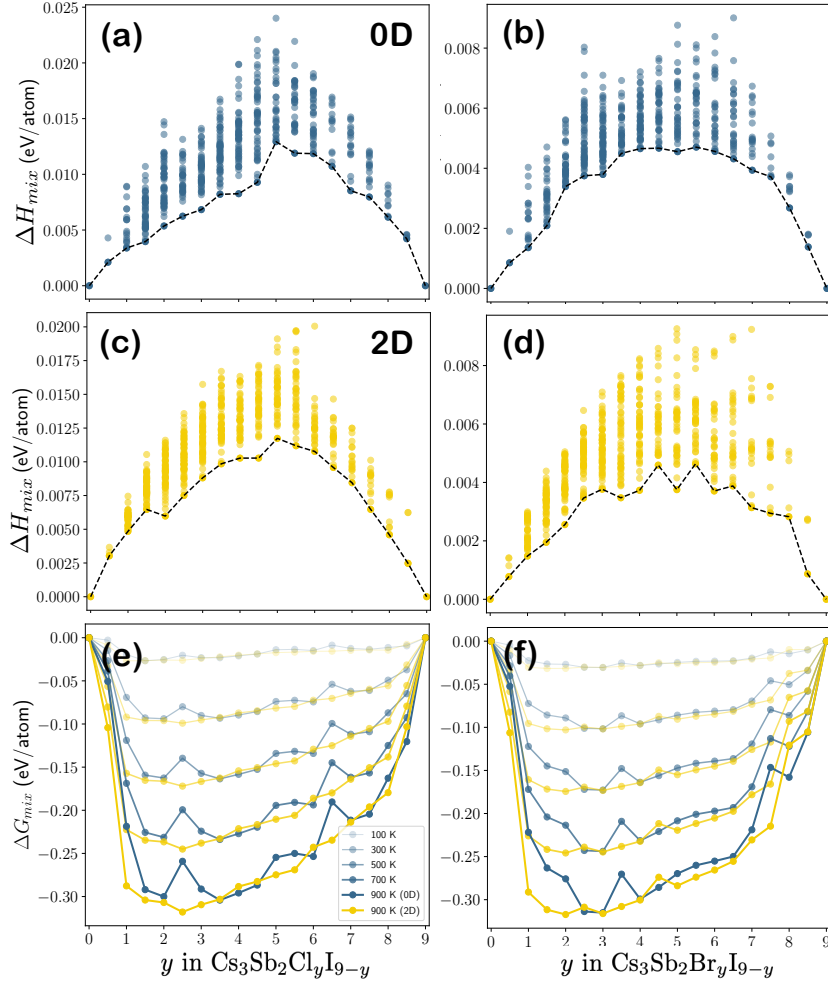
Figure 3: Composition–dependent mixing (a–d) enthalpies ΔH_{mix} and (e,f) free–energies ΔG_{mix} for 0D and 2D $Cs_3Sb_2X_yI_{9-y}$ solid solutions. In (a–d), each dot represents a random configuration of $Cs_3Sb_2X_yI_{9-y}$ being sampled, and the black dotted line corresponds to the lowest energy hull for ΔH_{mix}.

Harmonic phonon behaviour controlled by structural dimensionality

With the understandings on the thermodynamic stabilities of $Cs_3Sb_2X_yI_{9-y}$, we proceed to investigate their dynamic stabilities. In this section, we focus on the 0 K phononic properties of pure low–dimensional $Cs_3Sb_2X_9$ perovskites. Fig. 4 shows their harmonic phonon dispersion relationships, whereas the total and atom–resolved phonon density–of–states are shown in Fig. S1 of the Supporting Information (SI). Chemically, it is clear that all real phonon modes are generally stiffened from I to Br and then Cl, following the same trend as their formation energies (Fig. 2), since both phenomena are governed by the chemical bonding strengths.

Similar to many other perovskite materials, all 2D and 0D $Cs_3Sb_2X_9$ also exhibit dynamic instability as signified by the presence of phonon modes with negative frequencies. However, the lattice vibration
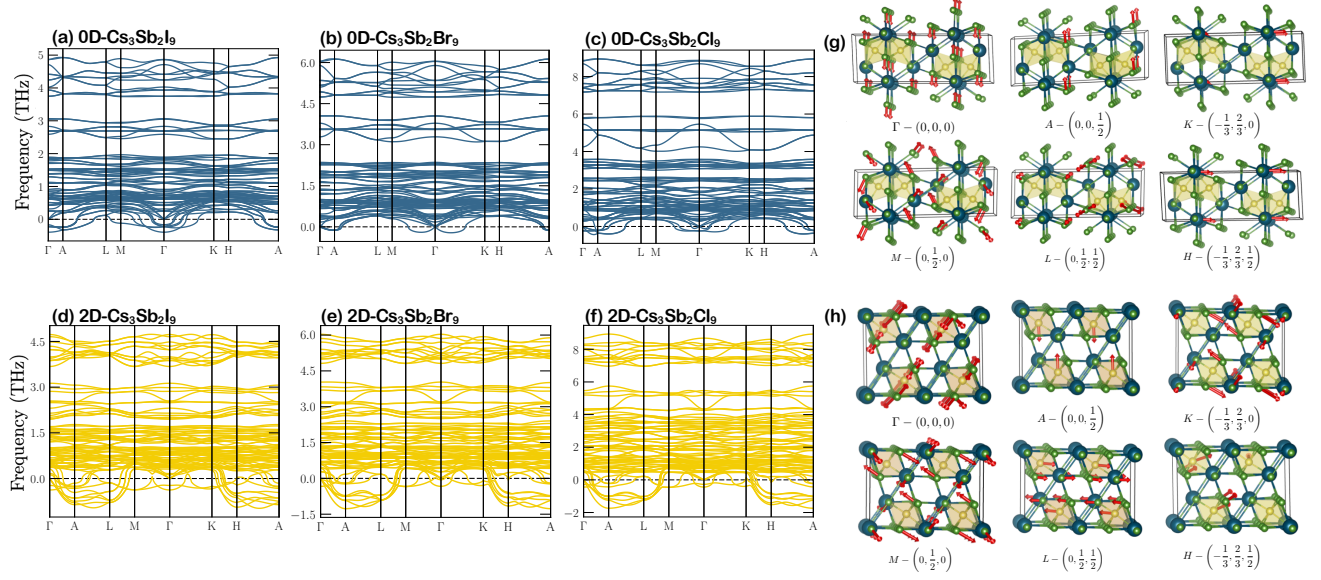
9

Figure 4: Harmonic phonon dispersion relationships for (a–c) 0D and (d–f) 2D $Cs_3Sb_2X_9$ perovskites. The softest vibrational modes at high–symmetry points for (g) 0D and (h) 2D $Cs_3Sb_2I_9$ are also displayed.

modes show distinctive differences as the structural dimensionality changes. Overall, 2D $Cs_3Sb_2X_9$ are found to be systematically softer than their 0D counterparts, as indicated by the presence of more negative phonon frequencies in their phonon dispersion relationships [Fig. 4(d–f)]. Moreover, the negative phonon frequencies for 2D $Cs_3Sb_2X_9$ are found to show a more pronounced decreasing trend as X changes from I to Cl, in comparison with their 0D counterparts. Overall, this suggests that, even though 2D perovskites are beneficial for charge transports in photovoltaic devices compared to 0D perovskites, they may suffer from larger electron–phonon scattering than 0D perovskites, which will be further examined in the subsequent sections.

We now examine the soft phonon modes in more detail. Γ (the ferroelectric instability) and A–point soft–phonons are found to be the two main contributors, with comparable strength, to the dynamic instabilities of 0D $Cs_3Sb_2X_9$. It is interesting to discover that $Cs_3Sb_2Br_9$ does not possess imaginary phonon mode at the Γ–point, but along the reciprocal space vectors pointing away from it. A small imaginary mode also occurs at the M–point in 0D–$Cs_3Sb_2I_9$ only. In 3D cubic perovskites, this corresponds to the dynamic instability induced by the motion of octahedral tilting. Analogously, in 0D–perovskite [Fig. 4(g)], each face–sharing SbX_6–octahedral dimer tilts as a single rigid structural unit, since the vibrational amplitudes on atoms in the octahedra–sharing faces are zero. This weakens the M–point instability in low–dimensional perovskites because an octahedron cannot tilt by itself independently. The tilting directions for the two octahedral dimers in one unit cell are opposite to each other, because these two dimers are symmetry–related by a translation and mirror reflection.

In stark contrast, for 2D $Cs_3Sb_2X_9$, structural instability contributed by the soft phonons at Γ– and M–points are much weaker than the other dominating contributions from soft–phonons at the A, L

and H points in the reciprocal space. It can be seen from Fig. 4(h), that, unlike 0D $Cs_3Sb_2I_9$, the off–center vibrations of Sb^{3+} ions in the SbX_6 octahedra also contribute to the vibrational instability at these high–symmetry points of 2D $Cs_3Sb_2I_9$. In particular, the softest vibrational mode at A–point is completely contributed by the off–center vibrations of Sb^{3+}, which appears to be out–of–phase for Sb^{3+} in a pair of face–sharing octahedra. The instabilities at the L, H and K are also unique in 2D perovskites, which do not exist in their 0D counterparts. As shown in Fig. 4(h), the soft modes at both L and H points appear to be an in–phase vibration of a Sb^{3+} cation together with their neighbouring X^- anions that are directly bonded to it, whereas the soft–mode at the K point corresponds to the titling movement in one of the two face–sharing SbI_6–octahedra within a unit cell.

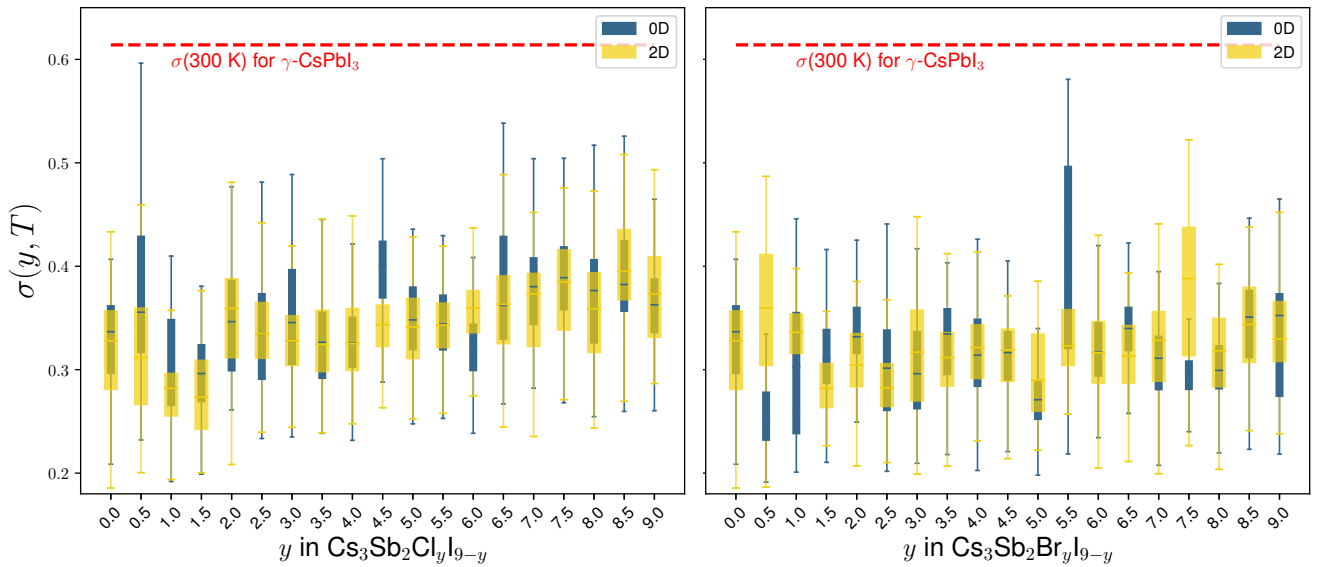## Composition–dependent structural dynamics at 300 K

Figure 5: Composition–dependent anharmonic scores (σ) for 0D and 2D (left) $Cs_3Sb_2Cl_yI_{9-y}$ and (right) $Cs_3Sb_2Br_yI_{9-y}$ solid solutions at 300 K. The anharmonic scores are calculated for every frame across the entire 1600 fs long MD trajectories. The box shows the distributions of σ values across an entire MD trajectory for a given composition. The box limits represent the 1st and 3rd quartiles, whereas the whiskers show the range of the σ values within $1.5\times$ the interquartile range of the box limits. As a reference, the red dashed line shows the mean σ value for the orthorhombic (γ) phase of $CsPbI_3$,[29] which is the stable phase of $CsPbI_3$ at 300 K.

Having inspected the phonon dispersion relationships for the low–dimensional antimony halide perovskites, we proceed to examine the composition and dimension dependent room–temperature structural dynamics of their mixed halide solid solutions. Fig. 5 shows this information, as measured by the anharmonicity scores σ [Eq. (1)] for both 0D and 2D $Cs_3Sb_2X_yI_{9-y}$ at 300 K. Here, σ is calculated for each MD frame by taking the standard deviation in atomic forces across all atoms in the supercell,

and each box in Fig. 5 shows the spread of σ values across one full MD trajectory at a given composition. As a reference, the mean σ value[29] for the stable γ–phase of CsPbI$_3$ at 300 K is also shown.

Physically, anharmonicity score $\sigma < 1$ indicates low vibrational anharmonicity and high phase stability.[28] This is reflected by γ–CsPbI$_3$ possessing a σ value around 0.6. Fig. 5 shows that, across both dimensionalities and all chemical compositions, the σ values for Cs$_3$Sb$_2$X$_y$I$_{9-y}$ are even lower than that of γ–CsPbI$_3$ at 300 K. As such, low–dimensional inorganic antimony–halide perovskites are of much higher dynamic stabilities compared with 3D lead–halide perovskites. The direct origin of these low $\sigma-$ values is related to the shape of the joint–probability distributions of total and anharmonic atomic forces sampled in an MD simulation. These are shown in Fig. 6 for each of the three elements in 0D Cs$_3$Sb$_2$I$_9$, which shows that irrespective to the magnitude of the total force F, the anharmonic components are all well confined within one standard deviation of the total force [$\sigma(F)$]. This is distinctively different from highly anharmonic crystals, such as cubic CsSnI$_3$, for which the same joint–probability distribution [Fig. 3 Ref. 29] showed large anharmonic forces even when the total forces on atoms vanished. At a more fundamental level, even though low–dimensional Cs$_3$Sb$_2$X$_9$ also possess imaginary harmonic phonon frequencies (Fig. 4), the integrated phonon density–of–states (Fig. S1 in SI) are very small at these frequencies, which means contributions from soft mode phonon vibrations are small in antimony halide perovskites, giving rise to low vibrational anharmonicities in these systems.
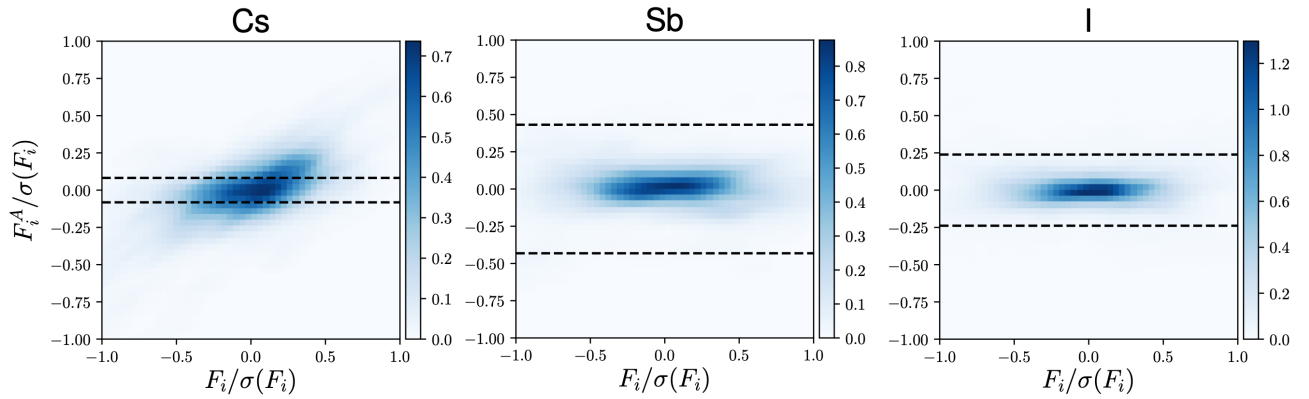

Figure 6: Joint–probability distributions of the total (F) and anharmonic (F^A) forces on the constituent atoms in 0D Cs$_3$Sb$_2$I$_9$ as obtained from DFT–MD sampling at 300 K. The distances between the two horizontal dash line is $2\sigma(F)$, the standard deviations in the total forces on a specific atom across the entire MD trajectory.

Fig. 5 further reveals that, at 300 K, the vibrational anharmonicities of Cs$_3$Sb$_2$X$_y$I$_{9-y}$ exhibit weak dimension and composition dependencies. This is also in stark contrast to the behaviour of lead–/tin–(mixed) halide perovskites where the degrees of vibrational anharmonicities depend strongly on their chemical contents.[29] In lead–/tin–halide perovskites, the valence band edge are contributed by the strong bonding orbitals originated from the ns^2 electrons from the B–site cation and the p–electrons of the halide anion. In contrast, the weak structural/chemical dependency in σ for Cs$_3$Sb$_2$X$_y$I$_{9-y}$ is caused

by a completely different electronic structure that underpins the chemical bonding in antimony–halide perovskites. As shown in the electronic density–of–states (DOS) for $Cs_3Sb_2I_9$ (Fig. 7), between -2 to 0 eV in the valence band, there exists only a vanishing hybridisation between Sb–s state and I–p near the band–edge, the $p - p$ hybridisation between Sb and I only contributed deep in the valence band or as anti–bonding orbitals in the conduction band. Therefore, the Sb–X bonds in $Cs_3Sb_2X_yI_{9-y}$ are expected to be weaker than Sn–X or Pb–X bonds in tin–/lead–halide perovskites, making the vibrational behaviours of low–dimensional $Cs_3Sb_2X_yI_{9-y}$ become less affected by chemical compositions and crystal structure.
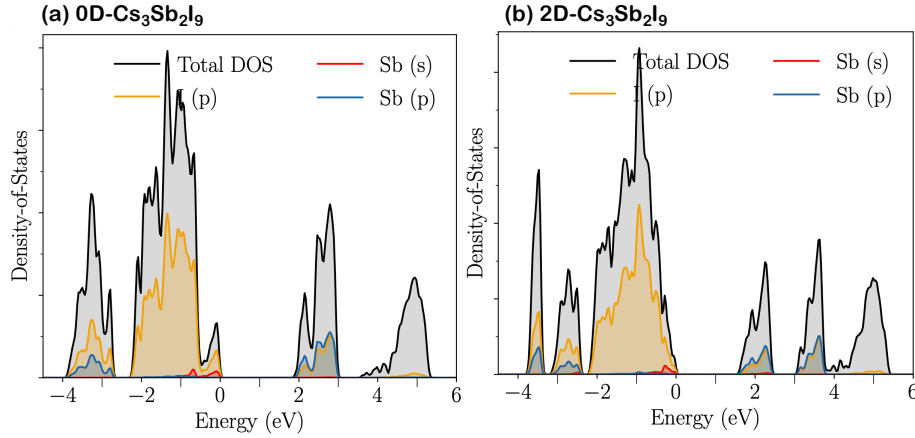

Figure 7: Electronic DOS for (a) 0D and (b) 2D $Cs_3Sb_2I_9$. Atomic contributions from Sb and I are also shown.

Composition and dimension dependent electronic structures

We now move on to discuss in detail, the electronic structures of low–dimensional $Cs_3Sb_2X_yI_{9-y}$ and the coupling with their ionic dynamics. As exemplified in the band structures [Fig. 8(left)], both 0D and 2D $Cs_3Sb_2I_9$ are indirect–band–gap semiconductors with their conduction band minimum at the Γ–point and valence band maximum located along the $\Gamma - K$ line in the reciprocal space. Nevertheless, for 0D $Cs_3Sb_2I_9$, the valence band maximum is much closer to the Γ point compared to its 2D counterpart, resulting in a small difference between the direct (E_g^{direct}) and indirect ($E_g^{indirect}$) band gap energies for 0D $Cs_3Sb_2I_9$.

Based on this understanding, we further examine the composition dependencies of E_g^{direct} and $E_g^{indirect}$ for $Cs_3Sb_2X_yI_{9-y}$ calculated from the structures with the lowest formation energies. As shown in Fig. 8(right), the composition and dimensionality show different effects on the band gap energies. Generally, the band gap energies for 2D $Cs_3Sb_2X_yI_{9-y}$ are lower than those for the 0D structures. It can be seen from Fig. 8(right) that the rate at which the band gap energies change with respect to the compositions (y) is primarily controlled by the chemical identity of halide X rather than the structural
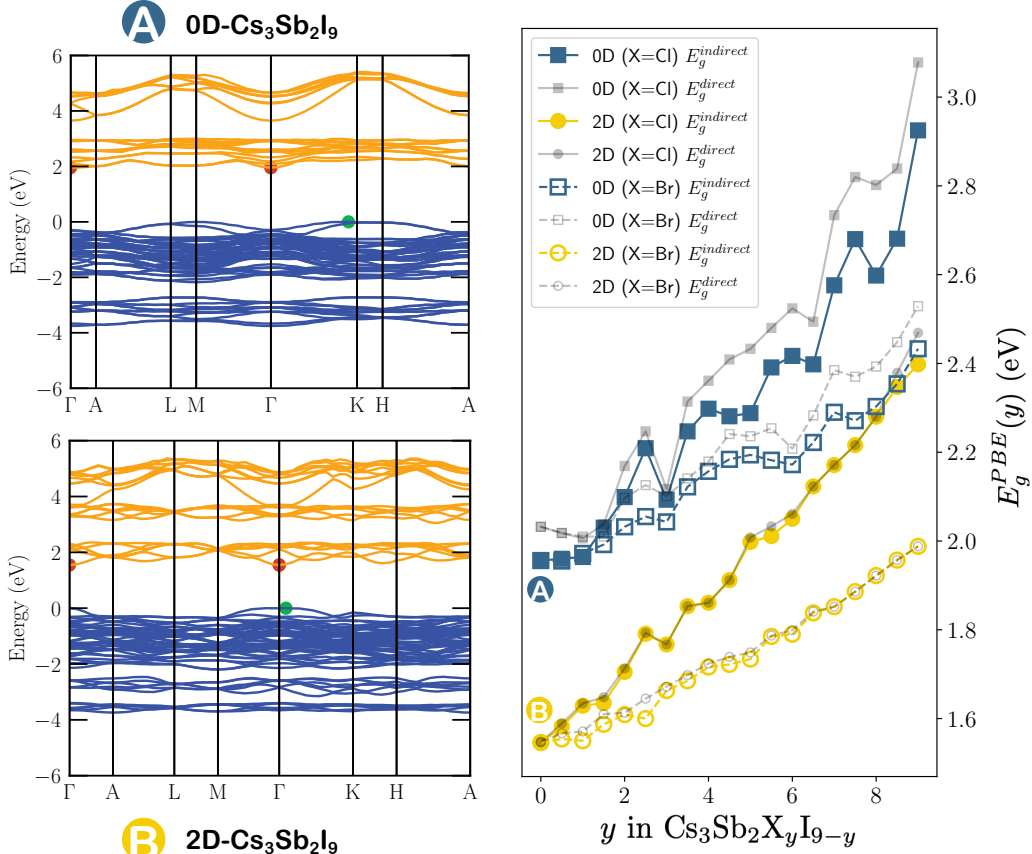
13

Figure 8: (Right) Composition–dependent direct and indirect electronic band gap energies for 0D and 2D $Cs_3Sb_2X_yI_{9-y}$ solid solutions. The electronic band structures for 0D and 2D $Cs_3Sb_2I_9$ are shown in the left panel, in which the band edge positions are indicated by the green and red dots, highlighting the nature of indirect band gaps in these materials.

dimensionality, with Cl/I intermixing leading to a much steeper increase in the band gap energies. This is because the magnitudes of the band gaps are determined by the overlaps of frontier atomic orbitals, which are dictated by the short–ranged chemical bonding environment in the perovskites. On the other hand, the differences between E_g^{direct} and $E_g^{indirect}$ do not show a strong dependency upon the chemical composition, but the crystal structure, with 0D $Cs_3Sb_2X_yI_{9-y}$ exhibits consistently large differences in E_g^{direct} and $E_g^{indirect}$ across the entire range of halide compositions. Such behaviour is correlated with the positions at which the band extrema appear in the reciprocal space, which is determined by the long–ranged crystal structure (dimensionality) of the material.

In perovskites, the vibration of ions can couple strongly with the electronic subsystem, which dictates their photo–physics at the operating temperature. Change in the structural dimensionality of materials, such as $Cs_3Sb_2I_9$, may also affect the strength of electron–phonon coupling in the system. Hence, it is interesting for us to further examine the dynamics of electronic band gaps at 300 K in low–dimensional antimony halide perovskites. Practically, due to the high computational costs associated with such an
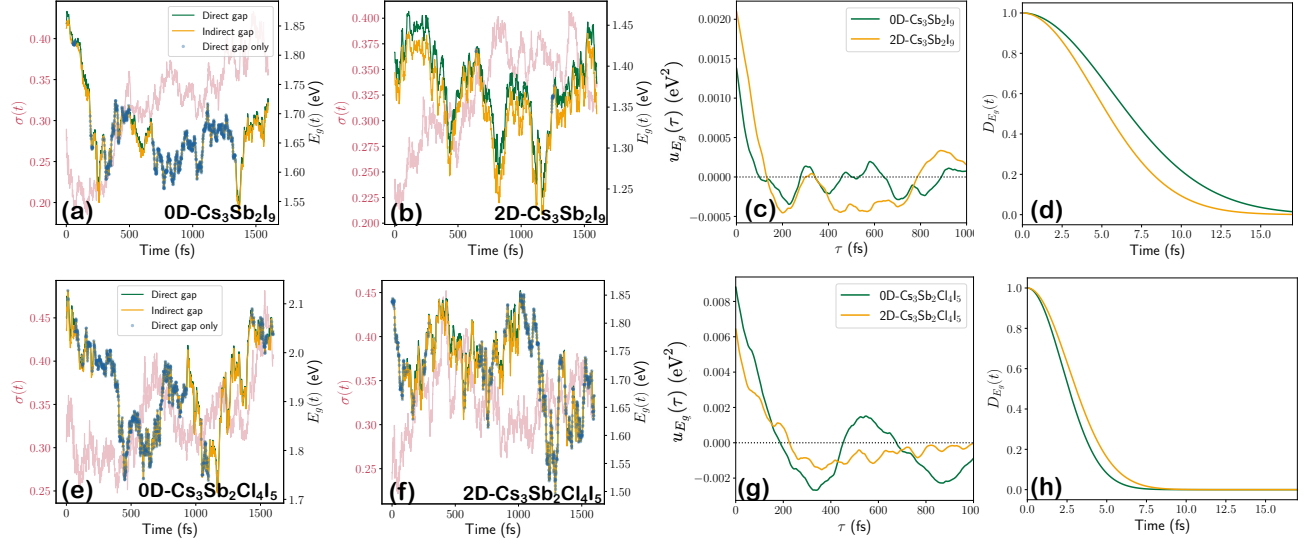
14

Figure 9: Band gap dynamics for low–dimensional (top) $Cs_3Sb_2I_9$ and (bottom) $Cs_3Sb_2Cl_4I_5$ at 300 K. The time–dependent evolution for the anharmonic scores (σ), direct and indirect band gaps of (a,e) 0D and (b,f) 2D antimony (mixed) halide perovskites are shown on the left–hand–side of the figure. Blue points indicate molecular dynamic frames at which only a direct band gap exists. The corresponding (c,g) time–dependent (direct) band gap autocorrelation functions $u_{E_g}(\tau)$ and (d,h) decoherence functions $D_{E_g}(t)$, which are extracted from the last 1100 fs of the MD trajectory, are shown on the right–hand–side of the figure.

investigation, we will only focus on the dimensional–dependent electron–phonon coupling behaviours in 0D and 2D pure $Cs_3Sb_2I_9$ and mixed halide $Cs_3Sb_2Cl_4I_5$, where the latter is experimentally found to be the composition with maximum Cl^- concentration at which a homogeneous solid solution is stable.

We first focus on the band gap dynamics of pure $Cs_3Sb_2I_9$. Fig. 9(a–b) plot the time–dependence of E_g^{direct} and $E_g^{indirect}$ for 0D and 2D $Cs_3Sb_2I_9$, respectively. In particular, we highlight MD snapshots at which ionic vibrations renormalise the indirect band gaps into direct ones. It is found here that thermal vibrations close the band gaps of low–dimensional $Cs_3Sb_2I_9$, which is opposite to inorganic lead/tin halide perovskites where thermal vibrations were shown to induce gap opening.[44] As such, thermal vibration could be beneficial for antimony halide perovskites in reaching the desirable absorption gaps for solar photovoltaics. Although the valence and conduction band extrema are further apart in the reciprocal space for 0D–$Cs_3Sb_2I_9$ compared to its 2D counterpart [Fig. 8], the trajectory in Fig. 9(a) shows that it is the 0D–$Cs_3Sb_2I_9$ that is most likely to have its indirect band gap being renormalised into a direct one by thermal vibrations, which could further benefit the material as lead–free absorber. For 2D $Cs_3Sb_2I_9$, on the other hand, the trend of $E_g^{direct}(t)$ closely follows that of $E_g^{indirect}(t)$, with E_g^{direct} being consistently larger than $E_g^{indirect}$ across the entire trajectory.

To further understand the interplay between ionic and electronic dynamics, in Fig. 9(a–b), we also show the time–evolution of the anharmonic scores $\sigma(t)$ for both structures in conjunction with their band

15

gaps. An anti–correlation between $\sigma(t)$ and $E_g(t)$ is immediately apparent, where band gap openings (closings) are typically observed in MD frames with low (high) vibrational anharmonicities. As high anharmonicity is associated with large–amplitude ionic vibration, it weakens the orbital overlaps between ions, which subsequently closes the band gaps. This shows that combining $\sigma(t)$ and $E_g(t)$ together can offer valuable insights into the complex interplays between structural and electronic dynamics in materials.

More information on the band gap dynamics can be extracted by calculating the band gap autocorrelation function, defined as

$$u_{E_g}(\tau) = \langle \Delta E_g(\tau) \Delta E_g(0) \rangle_T \tag{7}$$

where $\Delta E_g(t) = E_g(t) - \langle E_g(t) \rangle_T$, and $\langle \cdot \rangle_T$ is the averaged band gap across the entire MD trajectory. Here, we focus on the evolution of the direct band gap at Γ point only because of the high similarity in the values between the direct and indirect band gaps. Furthermore, the analysis is performed for the last 1.1 ps of the trajectories because the fluctuations in the band gap values tend to be more stabilised as shown in Fig. 9(a–b). Fig. 9(c) shows the band gap autocorrelations for 0D and 2D $Cs_3Sb_2I_9$ as functions of the delay time τ. At zero–time delay, $u_{E_g}(0) = \langle (\Delta E_g(t))^2 \rangle_T$, which reflects the averaged fluctuation of band gaps across the time series, and it is clear that the band gap fluctuations at 300 K is larger in the 2D structure of $Cs_3Sb_2I_9$. Similarly, the first encounter time at which the band gaps become completely decorrelated (~ 150 fs) are also found to be longer for 2D structure of $Cs_3Sb_2I_9$. Both observations provide indications of stronger electron–phonon coupling in 2D $Cs_3Sb_2I_9$, which is in line with the finding based on the harmonic phonons that the 2D $Cs_3Sb_2I_9$ is structurally 'softer'. Numerically, the band gap decoherence time can be more stably calculated[45] from the dephasing function $D_{E_g}(t)$, which can be obtained from $u_{E_g}(t)$ via a second–order cumulant expansion

$$D_{E_g}(t) = \exp \left[-\frac{1}{\hbar^2} \int_0^t \int_0^{t'} u_{E_g}(t'') dt'' dt' \right]. \tag{8}$$

As shown in Fig. 9(d), the decay of $D_{E_g}(t)$ is found to be faster in 2D $Cs_3Sb_2I_9$, further supporting the existence of stronger electron–phonon coupling in the system. By fitting the dephasing function to a Gaussian–type decay $g(t) = \exp[-1/2(t/\sigma_d)^2]$, the dephasing times σ_d for 0D and 2D $Cs_3Sb_2I_9$ is found to be 5.73 and 4.58 fs, respectively. These values are more than 2 times longer than those for $CsPb(I_xBr_{1-x})_3$ calculated based on the same approach,[43] which provides convincing evidence that the (reduced) vibrational anharmonicity and (weakened) electron–phonon couplings in low–dimensional antimony halide perovskites are strongly correlated with each other.

By repeating the similar analysis on 0D and 2D mixed halide $Cs_3Sb_2Cl_4I_5$ [Fig. 9(e–h)], the effects of halide intermixing on the band gap dynamics of low–dimensional antimony–halide perovskites can be further identified. It can be observed in Fig. 9(f) that renormalisation of indirect band gaps, which

16

are not observed in pure 2D $Cs_3Sb_2I_9$, are now more likely to occur in the mixed halide perovskites. The most profound change in the electronic dynamics is the significantly reduced band gap decoherence time σ_d for 2D (2.61 fs) and 0D (2.23 fs) $Cs_3Sb_2Cl_4I_5$ with the introduction of halide intermixings [Fig. 9(h)], indicating that the electron–phonon coupling in the mixed halide systems is strongly enhanced compared to the pure phase. This finding is consistent with our previous finding on the enhancement effect of electron–phonon coupling introduced by I/Br intermixing in cubic $CsPb(I_{1-x}Br_x)_3$.[43] Such effect arises primarily from the mismatch in the electronegativities between the two intermixing halide anions that are bonded directly to the B–site cations, hence reflects the changes in the short–ranged electronic interactions between the ions in the materials. This is supported by the fact that (a) vibrational anharmonicity σ is insensitive to both structural dimensionalities and compositions, and (b) the change in σ_d for perovskites with the same composition but different dimensionalities is also small. Both phenomena are dictated by the long–ranged structural characteristics of the materials.

Conclusions

To summarise, we have investigated computationally the thermodynamic stabilities, phononic/electronic properties and the dynamical interactions between them, for solid solutions of low–dimensional lead–free halide perovskites $Cs_3Sb_2X_yI_{9-y}$ (X=Cl and Br). It is found that Cl/I intermixing provides larger chemical pressure to stabilise the 2D polymorph of antimony halide perovskites at lower Cl concentration for enhancing charge transport properties in photovoltaic devices. In particular, entropy is found to be the dominant contribution that stabilises the homogeneous solid solutions, particularly at low Cl concentrations, which is consistent with the reported experimental result of synthesising 2D $Cs_3Sb_2Cl_yI_{9-y}$. All low–dimensional $Cs_3Sb_2X_yI_{9-y}$ solid solutions are found to be dynamically more stable at 300 K than the γ–phase of $CsPbI_3$. Consequentially, this reduces the electron–phonon coupling strength in $Cs_3Sb_2X_yI_{9-y}$ compared to cubic inorganic lead halides. More specifically, thermal vibrations is found to reduce the band gap in $Cs_3Sb_2I_9$, the 0 K band gaps of which are otherwise too large for solar–cell applications. Only 0D–$Cs_3Sb_2I_9$ are found to have its indirect band gap more likely to be renormalised into direct ones by ionic vibrations, however, its thermally renormalised band gap values are still larger than the optimum for solar photovoltaics.

Acknowledgements

References

(1) Kojima, A.; Teshima, K.; Shirai, Y.; Miyasaka, T. Organometal halide perovskites as visible-light sensitizers for photovoltaic cells. *J. Am. Chem. Soc.* **2009**, *131*, 6050.

(2) Zhou, H.; Chen, Q.; Li, G.; Luo, S.; Song, T.-b.; Duan, H.-S.; Hong, Z.; You, J.; Liu, Y.; Yang, Y. Interface engineering of highly efficient perovskite solar cells. *Science* **2014**, *345*, 542.

(3) others,, et al. Atomically thin two-dimensional organic-inorganic hybrid perovskites. *Science* **2015**, *349*, 1518.

(4) Babayigit, A.; Ethirajan, A.; Muller, M.; Conings, B. Toxicity of organometal halide perovskite solar cells. *Nature Mater.* **2016**, *15*, 247.

(5) Lyu, M.; Yun, J.-H.; Chen, P.; Hao, M.; Wang, L. Addressing Toxicity of Lead: Progress and Applications of Low-Toxic Metal Halide Perovskites and Their Derivatives. *Adv. Energy Mater.* **2017**, *7*, 1602512.

(6) Hao, F.; Stoumpos, C. C.; Cao, D. H.; Chang, R. P.; Kanatzidis, M. G. Lead-free solid-state organic–inorganic halide perovskite solar cells. *Nature Photonics* **2014**, *8*, 489.

(7) others,, et al. Lead-free organic–inorganic tin halide perovskites for photovoltaic applications. *Energy Environ. Sci.* **2014**, *7*, 3061.

(8) others,, et al. Lead-free germanium iodide perovskite materials for photovoltaic applications. *J. Mater. Chem.A* **2015**, *3*, 23829.

(9) Filip, M. R.; Giustino, F. Computational screening of homovalent lead substitution in organic–inorganic halide perovskites. *J. Phys. Chem. C* **2016**, *120*, 166.

(10) Park, H.; Mall, R.; Alharbi, F. H.; Sanvito, S.; Tabet, N.; Bensmail, H.; El-Mellouhi, F. Learn-and-match molecular cations for perovskites. *J. Phys. Chem. A* **2019**, *123*, 7323.

(11) Sun, Q.; Yin, W.; Wei, S.-H. Searching stable perovskite solar cell materials using materials genome techniques and high-throughput calculations. *J. Mater. Chem. C* **2020**, *8*, 12012.

(12) Yamada, K.; Sera, H.; Sawada, S.; Tada, H.; Okuda, T.; Tanaka, H. Reconstructive Phase Transformation and Kinetics of $Cs_3Sb_2I_9$ by Means of Rietveld Analysis of X-Ray Diffraction and ^{127}I NQR. *J. Solid State Chem.* **1997**, *134*, 319.

(13) Saparov, B.; Hong, F.; Sun, J.-P.; Duan, H.-S.; Meng, W.; Cameron, S.; Hill, I. G.; Yan, Y.; Mitzi, D. B. Thin-film preparation and characterization of $Cs_3Sb_2I_9$: A lead-free layered perovskite semiconductor. *Chem. Mater.* **2015**, *27*, 5622.

(14) Singh, A.; Boopathi, K. M.; Mohapatra, A.; Chen, Y. F.; Li, G.; Chu, C. W. Photovoltaic performance of vapor-assisted solution-processed layer polymorph of $Cs_3Sb_2I_9$. *ACS Appl. Mater. Interf.* **2018**, *10*, 2566.

(15) Akkerman, Q. A.; D'Innocenzo, V.; Accornero, S.; Scarpellini, A.; Petrozza, A.; Prato, M.; Manna, L. Tuning the optical properties of cesium lead halide perovskite nanocrystals by anion exchange reactions. *J. Am. Chem. Soc.* **2015**, *137*, 10276.

(16) others,, et al. Bandgap-tunable cesium lead halide perovskites with high thermal stability for efficient solar cells. *Adv. Energy Mater.* **2016**, *6*, 1502458.

(17) Dastidar, S.; Egger, D. A.; Tan, L. Z.; Cromer, S. B.; Dillon, A. D.; Liu, S.; Kronik, L.; Rappe, A. M.; Fafarman, A. T. High chloride doping levels stabilize the perovskite phase of cesium lead iodide. *Nano Lett.* **2016**, *16*, 3563.

(18) others,, et al. All inorganic halide perovskites nanosystem: synthesis, structural features, optical properties and optoelectronic applications. *Small* **2017**, *13*, 1603996.

(19) Bai, D.; Bian, H.; Jin, Z.; Wang, H.; Meng, L.; Wang, Q.; Liu, S. F. Temperature-assisted crystallization for inorganic $CsPbI_2Br$ perovskite solar cells to attain high stabilized efficiency 14.81%. *Nano Energy* **2018**, *52*, 408.

(20) others,, et al. Chlorine-incorporation-induced formation of the layered phase for antimony-based lead-free perovskite solar cells. *J. Am. Chem. Soc.* **2018**, *140*, 1019.

(21) Peng, Y.; Huq, T. N.; Mei, J.; Portilla, L.; Jagt, R. A.; Occhipinti, L. G.; MacManus-Driscoll, J. L.; Hoye, R. L.; Pecunia, V. Lead-Free Perovskite-Inspired Absorbers for Indoor Photovoltaics. *Adv. Energy Mater.* **2020**, 2002761.

(22) Paul, G.; Pal, A. J.; Larson, B. W. Structure, Morphology, and Photovoltaic Implications of Halide Alloying in Lead–Free $Cs_3Sb_2Cl_xI_{9-x}$ 2D–Layered Perovskites. *Solar RRL* **2021**, *5*, 2000422.

(23) Peng, Y.; Huq, T. N.; Mei, J.; Portilla, L.; Jagt, R. A.; Occhipinti, L. G.; MacManus-Driscoll, J. L.; Hoye, R. L.; Pecunia, V. Lead-Free Perovskite-Inspired Absorbers for Indoor Photovoltaics. *Adv. Energy Mater.* **2021**, *11*, 2002761.

(24) Hoke, E. T.; Slotcavage, D. J.; Dohner, E. R.; Bowring, A. R.; Karunadasa, H. I.; McGehee, M. D. Reversible photo-induced trap formation in mixed-halide hybrid perovskites for photovoltaics. *Chemi. Sci.* **2015**, *6*, 613.

(25) Yuan, Y.; Huang, J. Ion migration in organometal trihalide perovskite and its impact on photovoltaic efficiency and stability. *Acc. Chem. Res.* **2016**, *49*, 286.

(26) Cottingham, P.; Brutchey, R. L. Compositionally Dependent Phase Identity of Colloidal CsPbBr$_{3-x}$I$_x$ Quantum Dots. *Chem. Mater.* **2016**, *28*, 7574.

(27) Wang, Y.; Guan, X.; Chen, W.; Yang, J.; Hu, L.; Yang, J.; Li, S.; Kalantar-Zadeh, K.; Wen, X.; Wu, T. Illumination-Induced Phase Segregation and Suppressed Solubility Limit in Br-Rich Mixed-Halide Inorganic Perovskites. *ACS Appl. Mater. Interf.* **2020**, *34*, 38376.

(28) Knoop, F.; Purcell, T. A.; Scheffler, M.; Carbogno, C. Anharmonicity Measure for Materials. *Phys. Rev. Mater.* **2020**, *4*, 083809.

(29) Yang, J. Mapping temperature-dependent energy–structure–property relationships for solid solutions of inorganic halide perovskites. *J. Mater. Chem. C* **2020**, *8*, 16815.

(30) Ong, S. P.; Richards, W. D.; Jain, A.; Hautier, G.; Kocher, M.; Cholia, S.; Gunter, D.; Chevrier, V. L.; Persson, K. A.; Ceder, G. Python Materials Genomics (pymatgen): A robust, open-source python library for materials analysis. *Comput. Mater. Sci.* **2013**, *68*, 314.

(31) Kresse, G.; Furthmüller, J. Efficient iterative schemes for ab initio total-energy calculations using a plane-wave basis set. *Phys. Rev. B* **1996**, *54*, 11169.

(32) Perdew, J. P.; Burke, K.; Ernzerhof, M. Generalized gradient approximation made simple. *Phys. Rev. Lett.* **1996**, *77*, 3865.

(33) Kresse, G.; Joubert, D. From ultrasoft pseudopotentials to the projector augmented-wave method. *Phys. Rev. B* **1999**, *59*, 1758.

(34) Togo, A.; Tanaka, I. First principles phonon calculations in materials science. *Scr. Mater.* **2015**, *108*, 1.

(35) Peng, Y.; Li, F.; Wang, Y.; Li, Y.; Hoye, R. L.; Feng, L.; Xia, K.; Pecunia, V. Enhanced photo-conversion efficiency in cesium-antimony-halide perovskite derivatives by tuning crystallographic dimensionality. *Appl. Mater. Today* **2020**, *19*, 100637.

(36) Ma, J.; Wei, S.-H. Bowing of the defect formation energy in semiconductor alloys. *Phys. Rev. B* **2013**, *87*, 241201.

(37) Dalpian, G. M.; Zhao, X.-G.; Kazmerski, L.; Zunger, A. Formation and composition-dependent properties of alloys of cubic halide perovskites. *Chem. Mater.* **2019**, *31*, 2497.

(38) Skelton, J. M. Lattice dynamics of Pnma Sn(S$_{1-x}$Se$_x$) solid solutions: energetics, phonon spectra and thermal transport. *J. Phys. Energy* **2020**, *2*, 025006.

(39) Grau-Crespo, R.; Hamad, S.; Catlow, C. R. A.; De Leeuw, N. Symmetry-adapted configurational modelling of fractional site occupancy in solids. *J. Phys. Cond. Matter* **2007**, *19*, 256201.

(40) Skelton, J. M.; Burton, L. A.; Jackson, A. J.; Oba, F.; Parker, S. C.; Walsh, A. Lattice dynamics of the tin sulphides SnS_2, SnS and Sn_2S_3: vibrational spectra and thermal transport. *Phys. Chem. Chem. Phys.* **2017**, *19*, 12452.

(41) Dalpian, G. M.; Liu, Q.; Varignon, J.; Bibes, M.; Zunger, A. Bond disproportionation, charge self-regulation, and ligand holes in s- p- and in d-electron ABX_3 perovskites by density functional theory. *Phys. Rev. B* **2018**, *98*, 075135.

(42) Kent, P.; Zunger, A. Theory of electronic structure evolution in GaAsN and GaPN alloys. *Phys. Rev. B* **2001**, *64*, 115208.

(43) Yang, J.; Wang, Y.; Wu, T.; Li, S. Correlating the Composition-Dependent Structural and Electronic Dynamics of Inorganic Mixed Halide Perovskites. *Chem. Mater.* **2020**, *32*, 2470.

(44) Wiktor, J.; Rothlisberger, U.; Pasquarello, A. Predictive determination of band gaps of inorganic halide perovskites. *J. Chem. Phys. Lett.* **2017**, *8*, 5507.

(45) Hwang, H.; Rossky, P. J. An analysis of electronic dephasing in the spin-boson model. *J. Chem. Phys* **2004**, *120*, 11380.